

## Sound velocities of five minerals to mantle pressures determined by the sideband fluorescence method

A. CHOPELAS, H. J. REICHMANN,<sup>1</sup> and L. ZHANG<sup>2</sup>

Max Planck Institut für Chemie, Postfach 3060, 55020 Mainz, Germany

**Abstract**—Sound velocities determined from acoustic modes measured in the chromium sideband fluorescence of MgO to 37 GPa, MgAl<sub>2</sub>O<sub>4</sub> to 11 GPa, Al<sub>2</sub>O<sub>3</sub> to 62 GPa, YAG to 58 GPa, and pyrope to 52 GPa are presented. The pressure derivatives of the bulk and shear moduli obtained from our velocity measurements are in excellent agreement with those obtained from lower pressure ultrasonic measurements. Both shear and compressional velocities are linear with volume for all materials unless a phase change or change in compressional mechanism occurred. Such changes were observed for MgAl<sub>2</sub>O<sub>4</sub> and pyrope at 11 and 28 GPa, respectively. The velocity-volume slope is different for all materials but is smaller for minerals containing significant proportions of alumina, particularly for the shear velocity. A linear velocity-volume relationship means that the elastic or anharmonic contribution to the geophysically important parameter  $(\partial \ln \rho / \partial \ln v)_p$ , where  $\rho$  is the density and  $v$  is a sound velocity, must increase with depth.

### INTRODUCTION

In 1992, a new method for measuring sound velocities from fluorescence spectra to very high pressures in the diamond anvil cell was introduced (CHOPELAS, 1992). In that paper, sound velocities of MgO were obtained to 22 GPa which were later extended to 36 GPa (CHOPELAS, 1996). This method has been successfully tested on other oxides, namely Al<sub>2</sub>O<sub>3</sub> (alumina) to 63 GPa (ZHANG and CHOPELAS, 1994) and MgAl<sub>2</sub>O<sub>4</sub> (spinel) to 11 GPa (CHOPELAS, 1996). The precision of this method approaches that of ultrasonic techniques but allows measurements to much higher pressures. Both bulk and shear moduli calculated from the sound velocities determined by the sideband fluorescence method were in excellent agreement with those obtained by ultrasonic measurements to lower pressures.

The method consists of monitoring the acoustic modes found in the vibrational sidebands of a fluorescing cation doped into the host lattice. The method requires that a fluorescing transition metal cation with 3 *d* electrons, *e.g.*, Mn<sup>4+</sup>, Cr<sup>3+</sup>, or V<sup>2+</sup>, be doped into the lattice at an octahedral site; for all five minerals presented in this article, Cr<sup>3+</sup> was used. The *d* to *d* transition that creates the very sharp fluorescence is the <sup>2</sup>E<sub>g</sub> → <sup>4</sup>A<sub>2g</sub> transition, which is spin, symmetry, and orbitally forbidden (see CHOPELAS, 1996, for a discussion). This very sharp electronic transition is vibrationally assisted

by uneven or odd parity vibrations of the host lattice because it relaxes the symmetry forbidden selection rule. For Cr<sup>3+</sup> cations, both T<sub>1u</sub> and T<sub>2u</sub> lattice phonons irrespective of their location in the Brillouin zone appear in the spectrum. These lattice phonons, which include the acoustic modes, appear as 'sidebands' on the low and high energy sides of the sharp electronic transition at an energy removed from the pure electronic or no phonon line corresponding to the energy of the phonon.

This sideband method has several advantages over the more conventional methods, such as ultrasonic techniques, Brillouin scattering, or the newer impulse stimulated scattering technique. The experimental requirements are very simple, requiring only a laser, diamond cell, and single monochromator with a photomultiplier tube. Since the orientation of the sample in the cell does not affect the results, an irregularly shaped chip in any quasi-hydrostatic pressure medium suffices. The signal is strong and does not degrade, even at high pressures, so that very small samples can be used, thus making it easily possible to measure velocities to lower mantle pressures. The measured acoustic modes are spherically averaged which provides a means to directly determine spherically averaged velocities (discussed later). High symmetry minerals are easiest to analyze. The velocity measurements by the fluorescence method are made typically with uncertainties of 0.3 to 0.5%, compared to the slightly smaller uncertainties of 0.1% for ultrasonic techniques. There are also some disadvantages: the inability of this method to determine individual elastic constants, the interpretation of the sidebands may be ambiguous especially in lower symmetry compounds, temperatures are lim-

<sup>1</sup>Current address: Bayerisches Geoinstitut, Universität Bayreuth, D-95440 Bayreuth, Germany

<sup>2</sup>Current address: Institut für Mineralogie, Universität Marburg, Lahnberge, D-35043 Marburg, Germany

ited to a few (three to four) hundred degrees above ambient, and the introduction of small quantities of iron (<1%) into a mineral suppresses the fluorescence.

In this article, we present the pressure dependence of the sound velocities of five of the eight minerals measured by the sideband method in our laboratory. We show that the sound velocities for these five minerals are linear versus volume to compressions as low as 0.8, as long as the mineral does not undergo any phase changes, even for the more complex garnet structure, which does not compress isotropically. We also show that the velocity-volume dependence is much smaller for those minerals containing alumina, particularly for the shear velocities and that the linear velocity-volume relationship requires that  $(\partial \ln \rho / \partial \ln v)_T$  increase with increasing pressure. The geophysical implications of this result are discussed.

### EXPERIMENTAL DETAILS

Fundamentally, the experimental techniques for all five minerals were similar, the mineral was confined in a gasketed diamond anvil cell with ruby for pressure calibration and a quasi-hydrostatic pressure medium, either a methanol:ethanol mixture (to 20 GPa) or argon. All minerals except the  $\text{MgAl}_2\text{O}_4$  sample were synthesized with small quantities of  $\text{Cr}^{3+}$ ; typically about 0.1%. The composition of the natural  $\text{MgAl}_2\text{O}_4$  sample has been previously reported (CHOPELAS and HOFMEISTER, 1991). In the experiments over 20 GPa with MgO and  $\text{Al}_2\text{O}_3$ , the samples were heated with a  $\text{CO}_2$  laser until the surrounding argon was molten, thus providing a truly hydrostatic environment for these samples to the highest pressures of these respective studies. The experiments on spinel and garnet could not be conducted this way because these materials undergo phase changes above 20 GPa. Pressures were measured before and after recording the sample spectra; maximum differences observed did not exceed 1% of the confining pressure. The fluorescence spectra of all minerals were excited with a few mW of either the 488.0- or 514.5-nm line of an argon laser, which was kept to the minimum power needed in order to avoid heating the sample due to light absorption. No peak broadening or shifting due to heating was observed. The laser light entered the diamond cell at an incident angle of approximately  $25^\circ$  and was focused to approximately 10- $\mu\text{m}$  diameter in the sample. The signal was collected in a back-scattering geometry with an  $f/2$  lens and focused into the analyzing monochromator, either a double or single (used in the YAG experiments), which were equipped with photon counting detection systems. Typical spectral resolution was  $1 \text{ cm}^{-1}$ . All spectra were recorded in a climate controlled environment, with temperatures typically  $293 \pm 1 \text{ K}$ , in order to prevent drift in monochromator calibration.

### SPECTROSCOPY

In conventional vibrational spectroscopy, *i.e.*, Raman and infrared spectroscopy, the vibrational

modes that appear in the spectrum must be very near the Brillouin zone center, where the acoustic modes are zero, because the process that allows the mode to appear in the spectrum depends on the direct interaction of light with the vibrational mode, requiring the wave vector of the phonon to match that of the light. In fluorescence spectroscopy, it is the interaction of light with the electronic transition and not the vibration that creates the spectrum, thus eliminating the Brillouin zone restriction. The selection rules for determining the presence of a vibrational mode in a sideband spectrum requires that the vibration not have inversion symmetry, *i.e.*, that it is of odd parity. For  $\text{Cr}^{3+}$ , both  $T_{1u}$  and  $T_{2u}$  vibrations, including the acoustic modes, appear in the sidebands irrespective of their location in the Brillouin zone. If the modes in the sidebands were restricted to one point in the Brillouin zone, sharp peaks as found in Raman spectra would be found instead of the broad and sometimes diffuse peaks found in the sidebands (illustrated for all five minerals in Fig. 1). The  $\text{Cr}^{3+}$  fluorescence spectrum in a host crystal at a six-fold coordinated site consists of a sharp central 'no-phonon' line onto which the vibrational modes are symmetrically superimposed (see Fig. 1). The intensity of the sidebands on the high energy or anti-Stokes side of the spectrum is dependent on temperature similar to the anti-Stokes Raman spectra; the number of modes excited at a given frequency is given by the Boltzmann distribution function. The vibrational energy of the phonon equals its energy separation from the central peak. There is usually more than one sharp peak near the central peak, which is either due to the lifting of the degeneracy of the d-orbitals because the six-fold site is not perfectly cubic ( $R_2$  line) or the local lowering of site symmetry caused by the substitution of a trivalent cation impurity for a divalent host crystal cation (N-lines) requiring some nearby cation vacancies for charge compensation. The wavelengths of the electronic transition of interest in  $\text{Cr}^{3+}$  range from about 685 to 700 nm.

The sidebands are representative of the phonons of the unperturbed lattice because the frequencies of the sidebands are not measurably affected by the presence of the impurity by the comparison of the sideband frequencies in  $\text{MgO:Mn}^{4+}$ ,  $\text{Cr}^{3+}$ , or  $\text{V}^{2+}$  (GLASS and SEARLE, 1967; CHOPELAS, 1996) to those measured by inelastic neutron scattering (SANGSTER *et al.*, 1970). Furthermore, comparison of the pressure dependence of the Raman and infrared modes to the pressure dependence of the sideband modes in  $\text{MgAl}_2\text{O}_4$  revealed identical behavior for both types of phonon data (CHOPELAS and

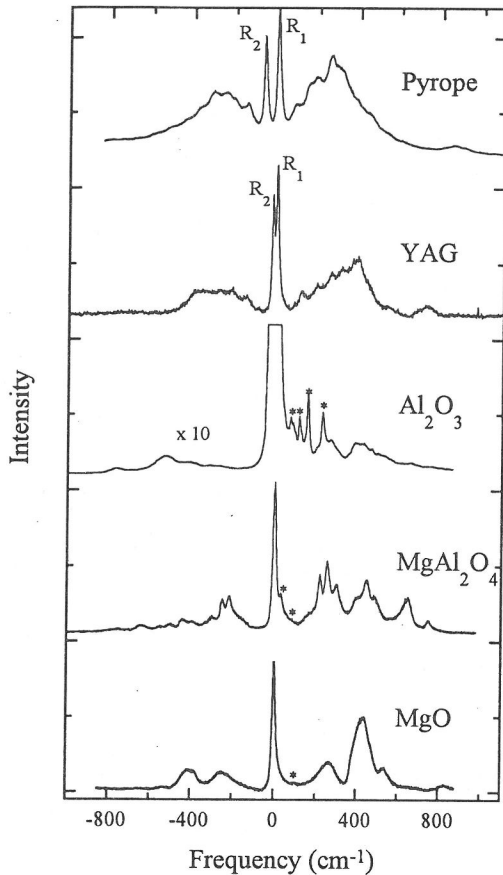


FIG. 1. The 1-atm fluorescence spectra of  $\text{Cr}^{3+}$  doped in the five minerals of this study. The  $R_1$  lines are set to zero to facilitate the comparison of the phonons of the various materials. The central peaks for these minerals are as follows:  $\text{MgO}$ —699.2 nm;  $\text{MgAl}_2\text{O}_4$ —685.5 nm;  $\text{Al}_2\text{O}_3$ —694.3 nm;  $\text{YAG}$ —688.8 nm; and pyrope—698.9 nm. The  $R_2$  lines for  $\text{YAG}$  and pyrope are well resolved and indicated in the figure. The sharp lines on the Stokes side of the central line in the  $\text{MgAl}_2\text{O}_4$  and  $\text{Al}_2\text{O}_3$  spectra are N-lines and are indicated by asterisks. The  $\text{Al}_2\text{O}_3$  vibrational sidebands are significantly weaker relative to the R lines at one atm so the spectrum is magnified by a factor of 10 to enhance the sidebands.

HOFMEISTER, 1991). Substitution of different impurity species affect the symmetries of the vibrations appearing in the sideband and hence intensities of the modes may vary. For example, the substitution of  $\text{V}^{2+}$  in  $\text{MgO}$  changes the appearance of the sidebands dramatically because the  $T_{1u}$  symmetry modes are strongly preferred over the  $T_{2u}$  modes (CHOPELAS and NICOL, 1982) but the positions of the modes are not shifted from those found in  $\text{Cr}^{3+}$  doped  $\text{MgO}$  (CHOPELAS, 1996).

In order to obtain the sound velocities from the

sideband spectra, the transverse and longitudinal acoustic modes need to be distinguished from the optical modes. Fortunately, the frequencies of the sideband modes closely correspond to those found in inelastic neutron scattering studies for  $\text{MgO}$  (SANGSTER *et al.*, 1970),  $\text{Al}_2\text{O}_3$  (KAPPUS, 1975), and  $\text{MgAl}_2\text{O}_4$  (THOMPSON and GRIMES, 1978) making assignment of the acoustic modes in the sidebands relatively straightforward. For the garnets, however, the large number of atoms in the unit cell means there are a large number of vibrations to be accounted for, complicating the acoustic mode assignment. Furthermore, two-phonon features may also appear in the sidebands although this doesn't seem to be the case for the other three compounds. There are other factors that can aid in distinguishing the acoustic modes from the optic aside from the fact that the acoustic modes are expected to be among the lowest in frequency in the spectrum. (1.) High pressure behavior can be used. In  $\text{MgO}$ ,  $\text{Al}_2\text{O}_3$  and  $\text{MgAl}_2\text{O}_4$ , the acoustic modes have much larger magnitude second pressure derivatives than the optic modes (CHOPELAS and HOFMEISTER, 1991; CHOPELAS, 1992; ZHANG and CHOPELAS, 1994; CHOPELAS, 1996). (2.) Process of elimination can be used. For example, in  $\text{MgAl}_2\text{O}_4$ , nearly all the optic modes in the sidebands could be accounted for by the infrared and Raman active modes, leaving the selection of the acoustic modes straightforward. (3.) Finally, the acoustic mode results can be verified with the low pressure sound velocity data from ultrasonic studies. In the  $\text{MgO}$ ,  $\text{Al}_2\text{O}_3$ , and  $\text{MgAl}_2\text{O}_4$  studies, using any of the optic modes for determining the velocities at high pressure did not yield results that even approached those found in ultrasonic studies.

## SOUND VELOCITIES

The sound velocities of a mineral are related to the slope of the dispersion curves near the Brillouin zone center,  $d\omega/dk$  where  $\omega$  is the mode frequency and  $k$  is the wavevector ( $= 2\pi/a$ , where  $a$  is the lattice constant). However, the measured frequencies, or the peak in the fluorescence spectrum, are near values that one expects at the Brillouin zone edge. It is again emphasized that the appearance of a phonon in the sideband has little to do with Brillouin zone location but is only governed by its symmetry. Indeed, in examining the sideband spectrum of  $\text{MgO}$  (Fig. 1), we see that the transverse acoustic mode at  $270 \text{ cm}^{-1}$  is very broad with intensity down to  $0 \text{ cm}^{-1}$ , which is the frequency of the acoustic mode at the zone center. Therefore, this spectral feature obtains intensity from phonons

throughout Brillouin zone, *i.e.*, from the center to the edge.

In order to extract sound velocity information from the frequencies in the spectra, we need to determine how this frequency relates to velocity. The simplest method to illustrate this is to use a simple diatomic 1-dimensional "lattice". The phonon frequencies of this "lattice" can be easily obtained in terms of the elastic constant  $C$  between atoms and the masses of the heavy and light atoms,  $m_1$  and  $m_2$ , respectively, by solving the equation of motion. For small values of  $k$  (*e.g.*, Chapter 4 in KITTEL, 1976), the acoustic frequencies are

$$\omega = \sqrt{\frac{2C}{m_1 + m_2}} \times ka \quad (1)$$

and at maximum  $k$ , the acoustic frequencies are

$$\omega = \sqrt{\frac{2C}{m_1}} \quad (2)$$

To determine the relationship between the slope of the acoustic mode dispersion curve at the zone center to an observed frequency at the zone edge, a linear extrapolation of the slope to the zone edge yields

$$\omega_D = \sqrt{\frac{2C}{m_1 + m_2}} \times \pi \quad (3)$$

where the subscript D refers to the Debye frequency, which is the frequency at the zone edge with a linear dispersion curve. The ratio of the slope to the zone edge frequency is

$$\frac{\text{slope}}{\omega} = \sqrt{\frac{m_1}{m_1 + m_2}} \times \frac{\pi}{2} \quad (4)$$

The ratio in Eqn. 4 above is an expression of constants and suggests that the velocity must be proportional to the measured frequency as expected for a continuous elastic medium.

$$v \propto \omega \times a \quad (5)$$

Aside from the measured frequencies  $\omega$ , this method requires the lattice constant versus pressure and the zero pressure sound velocities, which have both been measured for a great number of materials. Equation 5 implies that it is immaterial what the exact function is for the acoustic dispersion curve except that it must not change general form during compression. Because all of the materials under consideration are oxides, it is not expected that the acoustic dispersion curves will be irregularly shaped. In fact, the available inelastic neutron scattering data for MgO (SANGSTER *et al.*, 1970),

Al<sub>2</sub>O<sub>3</sub> (KAPPUS, 1975), and MgAl<sub>2</sub>O<sub>4</sub> (THOMPSON and GRIMES, 1978) show that for all three compounds the acoustic mode dispersion curves are nearly sinusoidal.

This simple one-dimensional model might suggest that the acoustic mode frequencies that we measured are directional and not spherically averaged. However, it has been recently shown for MgO and MgAl<sub>2</sub>O<sub>4</sub> that the acoustic modes in these materials do, in fact, yield spherically average velocities by comparison of the directional velocity information provided by ultrasonic data to those from our experiments (see Fig. 2ab) (CHOPELAS, 1996). The sideband frequencies are compared to frequencies calculated from directional velocities using  $\omega = \omega_0(v/v_0)(a_0/a)$ , where the variables with the subscript zero represent values at one atm. The spherically averaged velocities from the ultrasonic studies compare very well with the sideband frequency measurements. This same test for the two garnets and Al<sub>2</sub>O<sub>3</sub> yields similar results as for MgO and MgAl<sub>2</sub>O<sub>4</sub>, although not quite as decisively, because (1) the ultrasonic data for YAG (YOGURTCU *et al.*, 1980) and Al<sub>2</sub>O<sub>3</sub> (GIESKE and BARSCH, 1968) are only to very low pressures, thus extrapolation to over 50 GPa for comparison have very large uncertainties, and (2) the ultrasonic (WEBB, 1989) and impulse stimulated scattering (CHAI *et al.*, 1993) data for pyrope are for substantially different compositions.

## VELOCITY RESULTS

The primary plots of sideband spectra at various pressures and frequency versus pressure for MgO, MgAl<sub>2</sub>O<sub>4</sub>, and Al<sub>2</sub>O<sub>3</sub> have been published (CHOPELAS, 1992; ZHANG and CHOPELAS, 1994; CHOPELAS, 1996) so only the highlights and results are shown here for those compounds. The velocity-pressure and velocity volume relationships for all materials are listed in Table 1 and the comparison of the sound velocity of all materials versus pressure to PREM values are illustrated in Fig. 3.

### MgO and Al<sub>2</sub>O<sub>3</sub>

For MgO and Al<sub>2</sub>O<sub>3</sub>, no phase transitions or unusual phenomena occurred over the pressure ranges of these studies nor were they expected to occur (ZHANG and CHOPELAS, 1994; CHOPELAS, 1996). Above 20 GPa, the samples were heated until the surrounding argon melted providing a hydrostatic environment and eliminating the pressure uncertainties due to pressure gradients. The frequencies and thus the sound velocities calculated using Eqn.

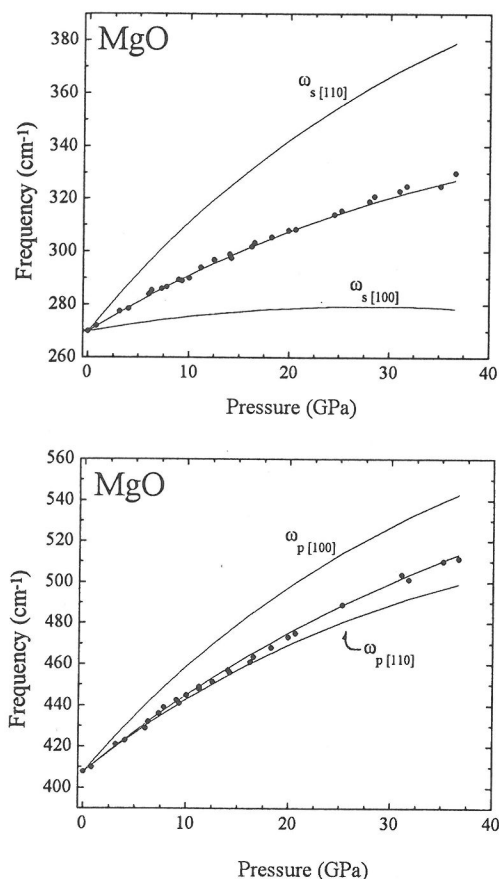


FIG. 2a. *Upper.* Comparison of the predicted effect that the directional shear velocities of MgO at high pressures would have on the transverse acoustic mode frequency to the actual frequencies measured at high pressure. The shear velocity in the 100 direction is calculated from  $(C_{44}/\rho)^{1/2}$  and in the 110 direction is calculated from  $\{(C_{11}-C_{22})/2\rho\}^{1/2}$ . The "directional" frequencies  $\omega$  at high pressure are then calculated from  $\omega_0 \times (v/v_0) \times (a_0/a)$ , where  $v$  are the respective directional velocities,  $a$  the lattice constant and the subscript zero represents the values at ambient pressure. The elastic constants used for these calculations are from ultrasonic studies (JACKSON and NIESLER, 1982; YONEDA, 1990). The intermediate curve that describes the data well is calculated using the averaged elastic moduli from those ultrasonic studies but with the second derivatives adjusted according to ultrahigh pressure compressional results (DUFFY and AHRENS, 1995).

FIG. 2b. *Lower.* Comparison of the predicted effect that the directional shear velocities of MgO at high pressures would have on the longitudinal acoustic mode frequency to the actual frequencies measured at high pressure. The compressional velocity in the 100 direction is calculated from  $(C_{11}/\rho)^{1/2}$  and in the 110 direction from  $\{(C_{11} + C_{12} + 2C_{44})/2\rho\}^{1/2}$ . The remaining information from Fig. 2a applies to this figure.

5 increased monotonically with pressure (see Fig. 3) and followed the trends expected by extrapolating the low pressure ultrasonic data. Plots of the velocity versus volume for both materials yielded straight lines (Fig. 4ab). For  $\text{Al}_2\text{O}_3$ , the large number of optic modes surrounding the longitudinal acoustic mode rendered it impossible to measure this mode to high pressures with any confidence (ZHANG and CHOPELAS, 1994). We were only able to measure two of the transverse acoustic modes, which exhibited identical behavior, and obtained a good constraint on the shear velocity to over 60 GPa. The compressional velocity was calculated using the well-constrained bulk modulus and its pressure derivative, the density, and our shear velocity from

$$\nu_p = \left[ \frac{K_S}{\rho} + \frac{4}{3} \times \nu_s^2 \right]^{1/2} \quad (6)$$

This method yielded reasonable results (Fig. 3 and 4ab).

#### *MgAl<sub>2</sub>O<sub>4</sub>*

For  $\text{MgAl}_2\text{O}_4$ , data were taken to 21 GPa (CHOPELAS and HOFMEISTER, 1991) but a change in compressional mechanism was observed as a break in slope for some of the optical modes in the Raman, infrared, and sideband spectra and as decreases in frequencies of the acoustic modes. Significant changes in the sideband fluorescence spectra were not observed until 19 GPa, where the signal became significantly weaker and the shape of the sidebands changed dramatically. Therefore, we report the sound velocities of  $\text{MgAl}_2\text{O}_4$  to only 11 GPa (CHOPELAS, 1996). It is noted here that the shear velocity does not change with pressure within the uncertainties of the data even though the compressional velocity behaves similarly to that of the other compounds.

#### YAG

Typical high pressure spectra of YAG {yttrium aluminum garnet:  $\text{Y}_3\text{Al}_2(\text{AlO}_4)_3$ } are shown in Fig. 5. It is clear that the signal quality or resolution does not degrade with pressure. It is also noted here that this sample was not heated at high pressures to relax the argon matrix but the resolution does not degrade substantially or suddenly with pressure. In these experiments, pressures were taken from ruby chips placed very close to the sample in order to minimize the uncertainties due to pressure gradients. The acoustic modes are indicated in Fig. 5 at

Table 1. Pressure and volume dependence of the sound velocities of MgO and MgAl<sub>2</sub>O<sub>4</sub>

Pressure Dependence in km/s	Volume Dependence in km/s
$v_s(P) = v_s(0) + (\partial v_s / \partial P)_T \cdot P + (\partial^2 v_s / \partial P^2) \cdot P^2$	$v_s = v_{s0} + \{ \partial v_s / \partial (V/V_0) \} \cdot (1 - V/V_0)$
<b>MgO</b>	
$v_s = 6.05(1) + 0.0381(13) \cdot P - 3.6(4) \cdot 10^{-4} \cdot P^2$	$6.05(1) + 6.37(10) \cdot (1 - V/V_0)$
$v_p = 9.70(2) + 0.0704(20) \cdot P - 5.6(6) \cdot 10^{-4} \cdot P^2$	$9.69(1) + 12.5(2) \cdot (1 - V/V_0)$
<b>MgAl<sub>2</sub>O<sub>4</sub></b>	
$v_s = 5.49(5) + 0.001(1) \cdot P$	$5.49(1) + 0.1(3) \cdot (1 - V/V_0)$
$v_p = 9.785(11) + 0.047(5) \cdot P - 0.0010(5) \cdot P^2$	$9.79(1) + 8.0(4) \cdot (1 - V/V_0)$
<b>Al<sub>2</sub>O<sub>3</sub></b>	
$v_s = 6.41(1) + 0.0234(11) \cdot P - 1.7(2) \cdot 10^{-4} \cdot P^2$	$6.40(3) + 5.70(13) \cdot (1 - V/V_0)$
$v_p = 10.90(11) + 0.0532 \cdot P - 1.9 \cdot 10^{-4} \cdot P^2$	$10.87 + 17.2 \cdot (1 - V/V_0)$
<b>YAG</b>	
$v_s = 4.94(2) + 0.00484(46) \cdot P$	$4.97(2) + 1.47(17) \cdot (1 - V/V_0)$
$v_p = 8.52(3) + 0.0520(26) \cdot P - 3.0(5) \cdot 10^{-4} \cdot P^2$	$8.52(1) + 11.3(2) \cdot (1 - V/V_0)$
<b>Pyrope</b>	
$v_s = 5.06(4) + 0.0271(22) \cdot P$	$5.07(1) + 6.5(5) \cdot (1 - V/V_0)$
$v_p = 9.16(4) + 0.0572(14) \cdot P$	$9.06(1) + 12.2(6)^\dagger \cdot (1 - V/V_0)$

<sup>†</sup>this value for pyrope is to 28 GPa; above here the slope changes to 20.1(11) (see fig. 8b)  
 Note: densities  $\rho_0$  in g cm<sup>-3</sup> and bulk moduli K in GPa of the minerals above are as follows-  
 MgO:  $\rho_0=3.583$ ,  $K=160.5$  (JACKSON and NIESLER, 1982); Al<sub>2</sub>O<sub>3</sub>:  $\rho_0=3.982$ ,  $K=253.0$  (GIESKE and BARSCH, 1968); MgAl<sub>2</sub>O<sub>4</sub>:  $\rho_0=3.578$ ,  $K=195.7$  (CHANG and BARSCH, 1973); YAG:  $\rho_0=4.550$ ,  $K=180.3$  (YOGURTCU *et al.*, 1980); Pyrope:  $\rho_0=3.601$ ,  $K=172.8$  (O'NEILL *et al.*, 1991); MgSiO<sub>3</sub> perovskite:  $\rho_0=4.096$ ;  $K=264.0$  (WEIDNER *et al.*, 1993)

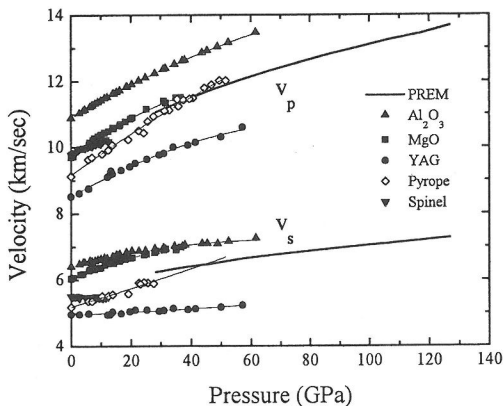


FIG. 3. Plot of compressional and shear velocities of five minerals versus pressure at room temperature. The data are indicated by the symbols and the fitted functions are listed in Table 1. The lower mantle PREM (DZIEWONSKI and ANDERSON, 1981) compressional and shear velocities at mantle pressure and temperatures are shown for comparison. Velocities for perovskite should lie slightly above those for Al<sub>2</sub>O<sub>3</sub> at  $v_{s0} = 6.58$  and  $v_{p0} = 11.1$  km/s (WEIDNER *et al.*, 1993).

194 and 319 cm<sup>-1</sup>. Justifications for these identifications are: (1) These are the only two modes that did not correlate to either an infrared or Raman mode (HURRELL *et al.*, 1968; HOFMEISTER and CAMPBELL, 1992), (2) the LA mode at 319 cm<sup>-1</sup> exhibited the largest magnitude second derivative, and (3) these frequencies yielded high pressure velocities consistent with the available ultrasonic data (YOGURTCU *et al.*, 1980). Moreover, these frequencies for YAG are very near those found for MgAl<sub>2</sub>O<sub>4</sub> and are therefore not unreasonable. The pressure dependencies are shown in Fig. 6a and their velocities calculated from Eqn. 5 are shown in Fig. 6b, with the uncertainties indicated in both of these figures. As in MgAl<sub>2</sub>O<sub>4</sub>, the shear velocity of YAG changes very little with pressure. The velocities of YAG are proportional to volume (Fig. 4ab) to the highest pressure of this study.

#### Pyrope

The velocity results for pyrope (Mg<sub>3</sub>Al<sub>2</sub>Si<sub>3</sub>O<sub>12</sub>) are preliminary but are worth mentioning here because they are of significant geophysical interest.

The sideband spectrum of pyrope (Fig. 1) strongly resembles that of YAG and the frequencies of most of the modes correspond well to the positions of the available infrared and Raman data (HOFMEISTER and CHOPELAS, 1991). As in the case of spinel, there appears to be a change in compressional mechanism or phase change at about 28 GPa in pyrope. First, the slope of the optical mode sideband at  $852\text{ cm}^{-1}$  decreases by about 45% at this pressure. Second, the resolution of the sideband spectra decreased suddenly above this pressure (Fig. 7). Since no Raman measurements exist to 28 GPa, we attempted to measure the Raman spectrum of this sample above this pressure but the inherently weak spectrum allowed us to monitor only four modes with any confidence. No discernible changes could be detected to 35 GPa. A similar decrease in resolution of sideband fluorescence spectra was observed for  $\text{MgSiO}_3$  majorite (CHOPELAS, 1991) at 38 GPa where the Raman spectrum exhibited dramatic changes, with major new peaks appearing which are characteristic of cubic garnets and peaks characteristic of the tetragonal structure disappeared.

A plot of velocity versus pressure from our results (Fig. 8a) shows that there is excellent agreement with impulse stimulated scattering data on a

different composition pyrope garnet (with 16% iron in the  $\text{Mg}^{2+}$  site) to 22 GPa (CHAI *et al.*, 1993) and, from this, it appears that these compressional velocity data can be simply extrapolated to higher pressures. However, a plot of velocity-versus volume reveals a break in slope for the velocity volume function at approximately 28 GPa (Fig. 8b), the same pressure the resolution of the spectra degraded. The transverse acoustic mode could not be followed with any confidence above this pressure due to this loss of resolution. The data scatter for pyrope is significantly higher than for the other materials so pyrope warrants another set of experiments before these results can be called final.

#### Pressure derivatives of the elastic moduli

The first and second pressure derivatives of the bulk and shear moduli can be estimated from the velocity results here from

$$K_s = \rho(v_p^2 - \frac{4}{3} \times v_s^2) \quad (7)$$

for the adiabatic bulk modulus and

$$G = \rho v_s^2 \quad (8)$$

for the shear modulus. The results for the elastic moduli versus pressure are fitted to

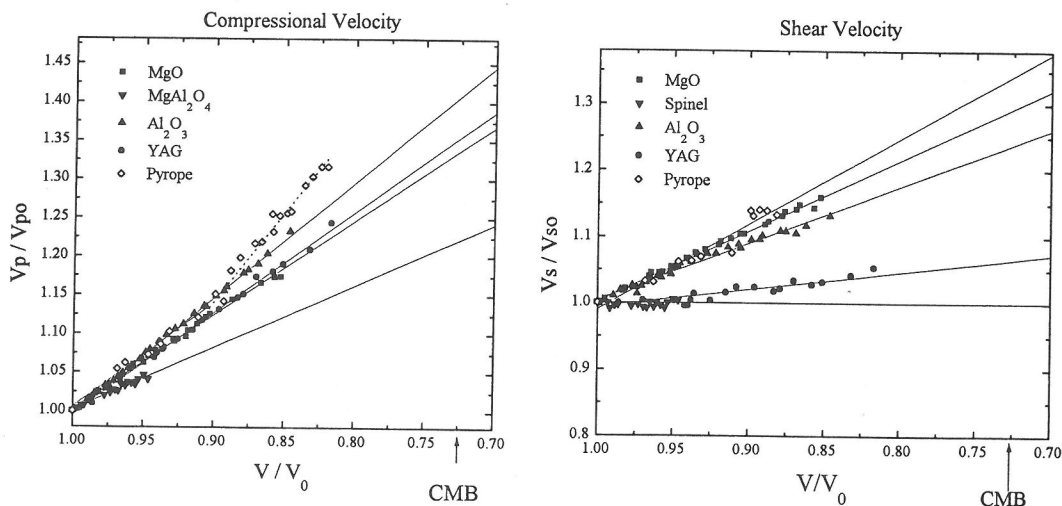


FIG. 4a. *Left*. Plot of reduced compressional velocity versus compression. The compression at the core mantle boundary (CMB) is indicated in the figure. The data are shown as symbols and the fitted lines are listed in Table 1 as velocity. The results for pyrope (open diamond) show an increase in slope at about  $V/V_0 = 0.9$  corresponding to 28 GPa (see Fig. 8b). Reduced volumes were calculated with a third-order finite strain equation of state (BIRCH, 1978) and bulk moduli listed in the footnote of Table 1 and pressure derivatives listed in Table 2.

FIG. 4b. *Right*. Plot of reduced shear velocity versus compression. The remaining information pertaining to Fig. 4a applies to this figure.

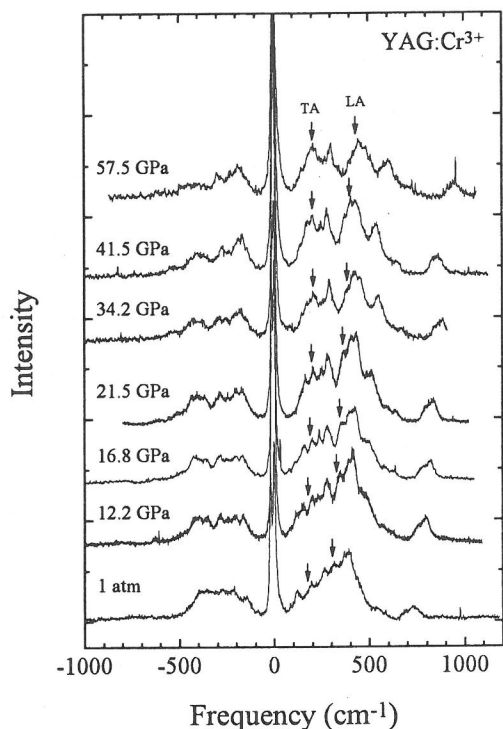
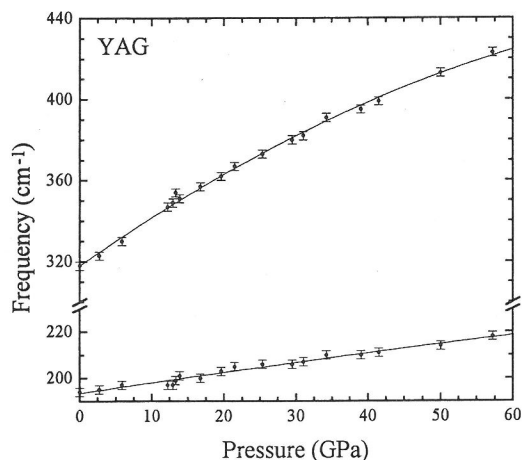


FIG. 5. Fluorescence spectrum of chromium-doped YAG at various pressures. The  $R_1$  line is set to  $0 \text{ cm}^{-1}$  in order to emphasize the pressure effect on the sidebands. The  $R_1$  line at  $688.8 \text{ nm}$  shifts at a rate of  $0.0385 \text{ nm/GPa}$ . The acoustic modes are indicated at each pressure. Note that the quality, intensity and resolution of the sidebands does not deteriorate even to the highest pressures.



$$M(P) = M_0 + M_0' \cdot P + \frac{1}{2} \times M_0'' \times P^2 \quad (9)$$

where  $M$  is the respective modulus. Since the density is required in the calculation of the moduli, the density is first calculated from a third order finite strain equation of state (BIRCH, 1978) with the zero pressure values of the bulk modulus obtained in ultrasonic studies or volume compressional studies (see Table 1). Then if the pressure derivative of the bulk modulus obtained here differed from that used to calculate the density, the volumes were recalculated with the new pressure derivative. This process was continued iteratively until the two results converged. Table 2 shows the excellent agreement between the low pressure ultrasonic results and our results for all five minerals.

## DISCUSSION

Comparison of the sound velocities of candidate minerals at high pressures and temperatures is the most definitive way to constrain compositional models of the mantle. Using density alone does not distinguish between the two most discussed lower mantle compositional models, a perovskitic model composed of almost entirely of  $\text{Mg}_{0.88}\text{Fe}_{0.12}\text{SiO}_3$  with minor percentages of other phases or a pyrolitic model composed primarily of magnesiowüstite and  $\text{MgSiO}_3$  perovskite where the iron is preferentially partitioned into the magnesiowüstite phase. Extrapolation of the densities of each of these three phases, the two different perovskite compositions and magnesi-

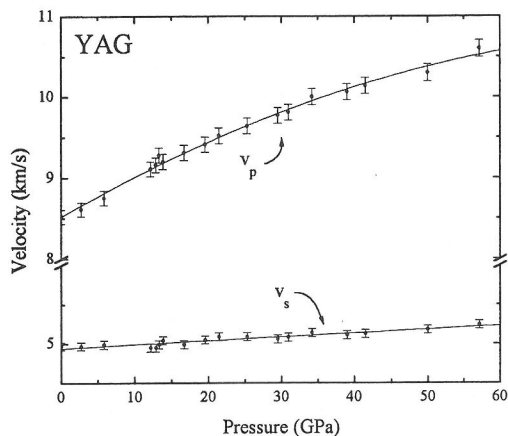


FIG. 6a. *Left*. The transverse and longitudinal acoustic modes of YAG at  $190$  and  $319 \text{ cm}^{-1}$ , respectively, versus pressure. The uncertainties indicated by the error bars are about  $0.5\%$ .

FIG. 6b. *Right*. The shear and compressional velocities of YAG calculated using Eqn. 5 and the frequencies shown in Fig. 6a. The lattice constant at each pressure was calculated with the third-order finite strain equation of state (BIRCH, 1978) and a bulk modulus of  $180.3 \text{ GPa}$  and its pressure derivative of  $5.2$ .

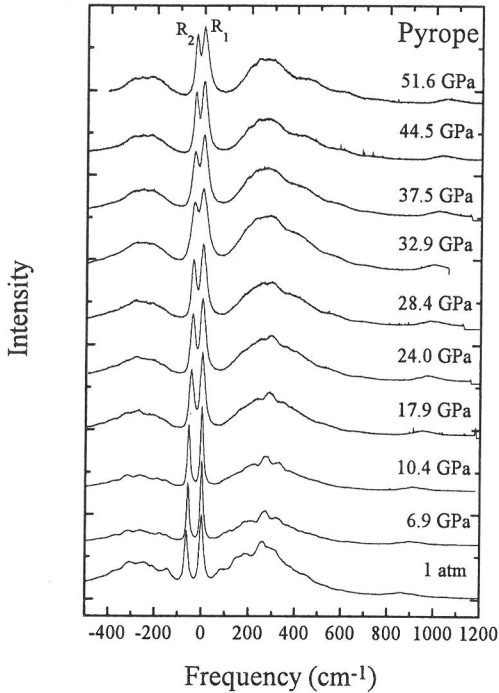


FIG. 7. Fluorescence spectra of pyrope ( $\text{Mg}_3\text{Al}_2\text{Si}_3\text{O}_{12}$ ) doped with chromium at various pressures. The  $R_1$  peak is plotted as  $0 \text{ cm}^{-1}$  in order to emphasize pressure induced changes in the sidebands. Note that above 28 GPa, the  $R_1$  and  $R_2$  lines and the features in the sidebands broaden substantially, decreasing the resolution markedly. Above this pressure, the transverse acoustic mode became impossible to resolve.

wüstite, to lower mantle conditions brings them to within 1–2 % of each other (CHOPELAS and BOEHLER, 1992) and to PREM densities for the lower mantle (DZIEWONSKI and ANDERSON, 1981). Using the bulk (hydrodynamic) sound velocity  $v_\phi$  from equations of state leads to less ambiguous results. However, for an adiabatic extrapolation to lower mantle conditions, the required high temperature values of the bulk modulus or its pressure derivative for perovskite are not very accurately known (and are current subject for debate) nor can they be measured at 1 atm or low pressures because of metastability problems. Bulk sound velocity can not yet be used as a much more rigorous constraint than the density.

To illustrate the difference between density and velocity comparison, the density of the mantle minerals and alumina versus pressure are plotted in Fig. 9, where we see the density these minerals converge at high pressures. The differences between  $\text{MgO}$  and  $\text{MgSiO}_3$  perovskite become smaller at high temperatures because of their respective thermal expansion coefficients. However, in examining Fig. 3 where the velocities measured here are shown relative to PREM, there are differences of at least 10% in velocities instead of differences less than 5% (for density) at room temperature. The perovskite velocities are expected to lie slightly above those for alumina with the 1 atm values at 6.58 and 11.1 km/s for  $v_s$  and  $v_p$ , respectively (WEIDNER *et al.*, 1993). Distinguishing the

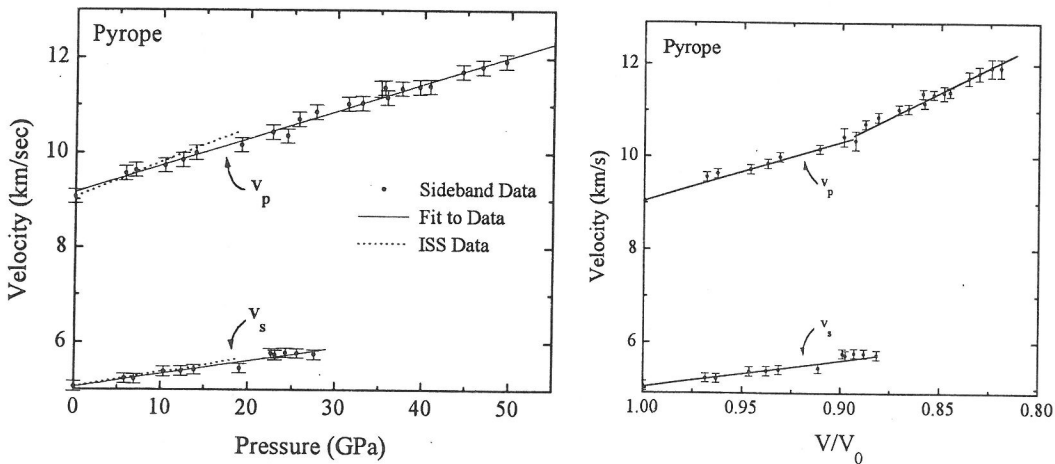


FIG. 8a. *Left*. Preliminary velocity results for pyrope for the compressional and shear velocity versus pressure. The pressure dependence of impulse stimulated scattering data for a slightly different composition garnet  $\{(\text{Mg}_{0.84}\text{Fe}_{0.16})_3\text{Al}_2\text{Si}_3\text{O}_{12}\}$  to 22 GPa (CHAI *et al.*, 1993) are shown for comparison.

FIG. 8b. *Right*. Plot of the pyrope shear and compressional velocities from Fig. 8a versus compression. The increase in slope of  $v_p$  versus  $V/V_0$  by over 60% at 28 GPa is clearly shown (see Table 1).

Table 2. Comparison of pressure derivatives of the elastic moduli obtained by the sideband method to those obtained by ultrasonic techniques.

		Sideband	Ultrasonics <sup>a</sup>	Reference
MgO	P <sub>max</sub> (GPa)	36.5	3.2	JACKSON and NIESLER, 1982
	K'	4.08	4.13	YONEDA, 1990
	K'' (GPa <sup>-1</sup> )	-0.036	-0.022	DUFFY and AHRENS, 1995
	G'	2.56	2.53	
	G'' (GPa <sup>-1</sup> )	-0.030	-0.027	
YAG	P <sub>max</sub> (GPa)	57.5	0.3	YOGURTCU <i>et al.</i> , 1980
	K'	5.16	4.44	
	K'' (GPa <sup>-1</sup> )	-0.0036	--	
	G'	0.68	0.62	
MgAl <sub>2</sub> O <sub>4</sub>	P <sub>max</sub> (GPa)	11.0 <sup>†</sup>	1.0	CHANG and BARSCH, 1973
	K'	5.05	5.15	YONEDA, 1990
	K'' (GPa <sup>-1</sup> )	-0.13	-0.48	
	G'	0.072	0.51	
Al <sub>2</sub> O <sub>3</sub>	<sup>@</sup> P <sub>max</sub> (GPa)	53.0	1.0	GIESKE and BARSCH, 1968
	G'	1.94	1.98	
	G'' (GPa <sup>-1</sup> )	-0.02	-0.02	
Pyrope	P <sub>max</sub> (GPa)	28.0 <sup>†</sup>	3.2	WEBB, 1989
	K'	4.5	4.7*	
	G'	1.73	1.81*	

<sup>a</sup>See Fig. 2a for explanation of values for MgO.

<sup>@</sup>Only shear velocities were measured.

<sup>†</sup>phase change or change in compressional mechanism at this pressure

\*pyrope with 36% iron at the Mg<sup>2+</sup> site

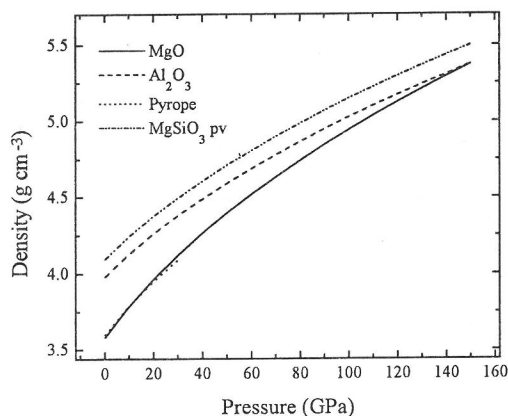


FIG. 9. The extrapolated densities of MgO, Al<sub>2</sub>O<sub>3</sub>, pyrope, and MgSiO<sub>3</sub> perovskite versus pressure at room temperature to the core-mantle boundary pressure. The MgO and MgSiO<sub>3</sub> perovskite curves converge even further at high temperatures because of the lesser value of  $\alpha$  for perovskite and the greater value of  $\alpha$  for MgO at high pressures. The densities at high pressure were calculated with the third-order finite strain equation of state (BIRCH, 1978) and the bulk modulus data listed in Tables 1 and 2. The density and bulk modulus values used for perovskite are listed in the Table 1 footnote with  $K_{OT}' = 4$  assumed.

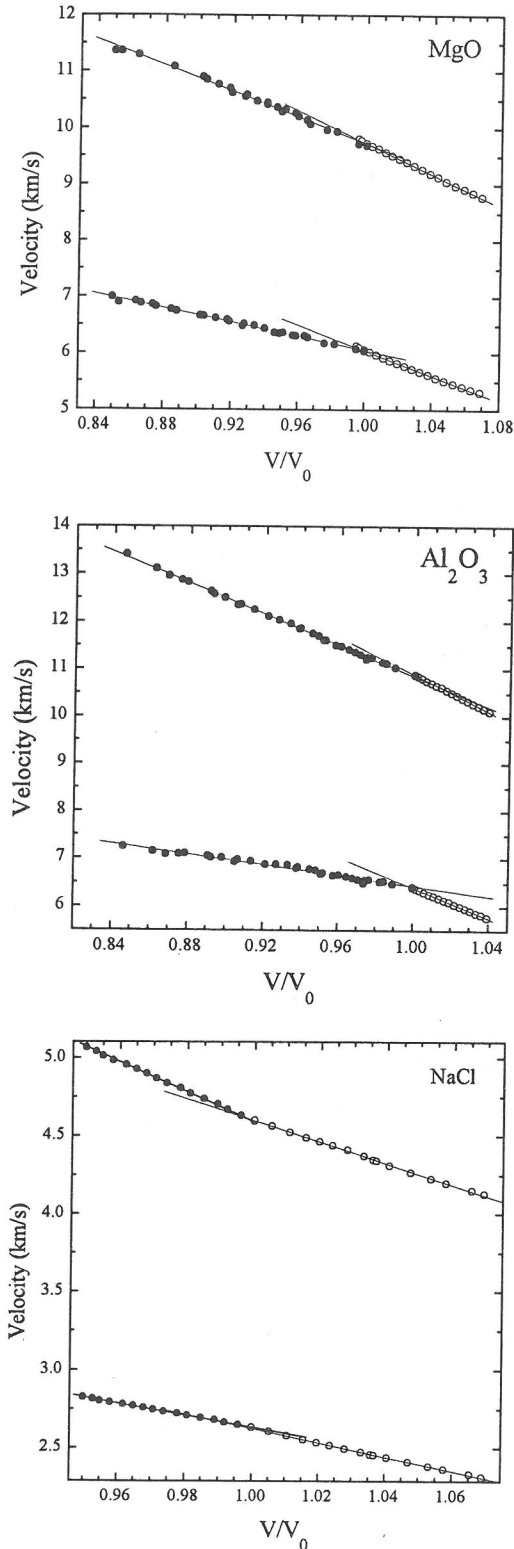
compositional models of the mantle will have to wait, however, until high pressure measurements for perovskite are completed.

$$(\partial \ln \rho / \partial \ln v)$$

Aside from distinguishing between mantle compositional models, measurements of sound velocities to these high pressures allows us to examine more closely the velocity-volume relationship for oxide minerals. This relationship in its logarithmic form is useful for interpreting lateral velocity anomalies in terms of lateral temperature anomalies from

$$\delta T = \frac{(\partial \ln \rho / \partial \ln v)_P}{\alpha} \times \delta v \quad (10)$$

where  $\delta v$  is the velocity anomaly,  $\alpha$  the thermal expansion coefficient, and  $\rho$  the density. {Note:  $\ln(\rho/\rho_0) = -\ln(V/V_0)$ .} Eqn. 10 assumes that the velocity variation is due to a temperature variation. Furthermore, note here that Eqn. 10 requires the isobaric value of  $(\partial \ln \rho / \partial \ln v)$  and our measurements yield the isothermal value. The following



discussion provides constraints for the high pressure isobaric ( $\partial \ln \rho / \partial \ln v$ )<sub>P</sub>.

As seen in Fig. 4ab, all the sound velocities depend linearly on volume as long as there is no change in compressional mechanism. It is also noted that the minerals with high alumina content have the smallest relative changes in shear velocity with compression. In fact,  $MgAl_2O_4$  exhibited no measurable change in shear velocity over the pressure range of that study. From examination of this figure, it is further clear that the velocity-volume relationship is quite different for all the materials particularly for the shear velocity. For compressional velocity, the variation of slope between minerals is much less but nonetheless, extrapolation of velocity to high pressures using this method requires at least some lower pressure data in order to establish the velocity-volume function.

The linear relationship between velocity and volume requires that the value of  $(\partial \ln \rho / \partial \ln v)$ <sub>T</sub> increases with pressure. Likewise, in the available data on sound velocities versus temperature {summarized in (ANDERSON *et al.*, 1992)}, there is a linear velocity-volume dependency for MgO and  $Al_2O_3$  (see Fig. 10a,b) although the slope is of different magnitude than that versus pressure at con-

FIG. 10a. *Top*. Plot of shear and compressional velocities of MgO ( $\Theta_D = 945$  K) versus reduced volume from high pressure data at room temperature (solid points are data from this study) and from high temperature data at 1 atm (open points are fitted values from (ISAAK *et al.*, 1989)). The slopes of the high temperature data for  $v_s$  and  $v_p$  are 11.1 and 14.0 km/s, respectively, compared to 6.4 and 12.5 km/s for the high pressure data (Table 1).

FIG. 10b. *Center*. Plot of shear and compressional velocities of  $Al_2O_3$  ( $\Theta_D = 1034$  K) versus reduced volume from high pressure data at room temperature (solid points are data from this study) and from high temperature data at 1 atm (open points are fitted values from (GOTO *et al.*, 1989)). The slopes of the high temperature data for  $v_s$  and  $v_p$  are 15.8 and 19.6 km/s, respectively, compared to 5.5 and 16.3 km/s for the high pressure data (Table 1).

FIG. 10c. *Bottom*. Plot of shear and compressional velocities of NaCl ( $\Theta_D = 321$  K) versus reduced volume from high pressure data at room temperature (solid points are fitted values from (SPETZLER *et al.*, 1972)) and from high temperature data at 1 atm (open points are data from (YAMAMOTO *et al.*, 1987)). The slopes of the high temperature data for  $v_s$  and  $v_p$  are 4.6 and 6.9 km/s, respectively, compared to 3.8 and 9.4 km/s for the high pressure data. Recent very high pressure data obtained by Brillouin scattering (CAMPBELL and HEINZ, 1992) yielded approximately 6.7 km/s for  $v_p$  versus reduced volume at room temperature. Compressional velocity versus reduced volume for KCl ( $\Theta_D = 235$  K) is 6.3 km/s at 1 atm and high temperature (YAMAMOTO and ANDERSON, 1987) and is 6.2 km/s at room temperature and high pressure (CAMPBELL and HEINZ, 1992).

stant temperature. This linearity versus temperature requires that  $(\partial \ln \rho / \partial \ln v)_P$  decreases with increasing temperature. Note that for both of these compounds the velocity-volume slope for the compressional velocity is very nearly the same whereas there are substantial differences for the shear velocity. In order to draw some conclusions on the required isobaric value of  $(\partial \ln \rho / \partial \ln v)$  at mantle conditions, its relationship to the isothermal value needs to be clarified.

The relationship between the isothermal and isobaric values of  $(\partial \ln \rho / \partial \ln v)$  can be obtained from straightforward mathematics

$$\left( \frac{\partial \ln \omega}{\partial T} \right)_v = \alpha \left[ \left( \frac{\partial \ln \omega}{\partial \ln \rho} \right)_T - \left( \frac{\partial \ln \omega}{\partial \ln \rho} \right)_P \right] \quad (11)$$

The first term the right hand side of the equation can be related to  $(\partial \ln v / \partial \ln \rho)_T$  by taking the natural log on both sides of Eqn. 5 and differentiating with respect to  $\ln \rho$  at constant temperature. This results in  $(\partial \ln v / \partial \ln \rho)_T = (\partial \ln \omega / \partial \ln \rho)_T - 1/3$  and when the same is done at constant pressure, it results in  $(\partial \ln v / \partial \ln \rho)_P = (\partial \ln \omega / \partial \ln \rho)_P - 1/3$ . Therefore,  $(\partial \ln v / \partial \ln \rho)_{T,P}$  may be directly substituted in Eqn. 11 above for  $(\partial \ln \omega / \partial \ln \rho)_{T,P}$  which then shows that the difference between the isobaric and the isothermal derivatives is directly related to the intrinsic anharmonicity  $(\partial \ln \omega / \partial T)_v$ . We do have evidence that the intrinsic harmonicity vanishes at lower mantle conditions (see following discussion), and thus, the differences between the isobaric and isothermal derivatives also vanishes. Note that the values of  $(\partial \ln v / \partial \ln \rho)$  lie between  $1/2$  and 2 therefore taking the inverse of these also gives us values that lie between  $1/2$  and 2. Thus, small differences between  $(\partial \ln v / \partial \ln \rho)$  values mean that  $(\partial \ln \rho / \partial \ln v)$  must approach each other as their inverses do.

The evidence that the intrinsic anharmonicity diminishes substantially at temperatures above the Debye temperatures is theoretically (HARDY, 1980) and experimentally based (ANDERSON *et al.*, 1992). In high temperature experiments on several minerals including  $\text{Al}_2\text{O}_3$ ,  $\text{MgO}$ , and pyrope, ANDERSON *et al.* (1992) showed that thermal pressure is linear with temperature above the Debye temperature  $\Theta_D$ , meaning intrinsic anharmonicity could not be detected. Furthermore, the velocity-volume functions of two alkali halides,  $\text{KCl}$  and  $\text{NaCl}$ , are nearly the same at room pressure and temperature (which is near or above the Debye temperatures of these materials, Fig. 10c). This means that the isobaric and isothermal derivatives of  $(\partial \ln \rho / \partial \ln v)$  are nearly the same as well.

We have clues as to what  $(\partial \ln \rho / \partial \ln v)_T$  should be at the high temperatures and pressures of the lower mantle by examining the PREM adiabatic values, which should be very near the isothermal values (shown in Fig. 11). These values are very similar to the values found for the mantle materials at room temperature and high pressure of about 1.0 for  $v_P$  and 1.4 for  $v_S$ , which are approximately double those found for  $(\partial \ln \rho / \partial \ln v)_P$  at room temperature and 1 atm (ANDERSON *et al.*, 1992) for a large number of minerals.

In summary, the value of the elastic (or anharmonic) contribution to  $(\partial \ln \rho / \partial \ln v)_P$  appears to increase from the reported 1-atm values as pressure increases. In examining Eqn. 10, the combined effect of  $(\partial \ln \rho / \partial \ln v)_P$  increasing and thermal expansivity decreasing with depth implies that the same magnitude velocity anomalies at greater depths yields larger temperature anomalies. Thus, the structural features in terms of velocity anomalies found in three-dimensional tomographic models significantly change when put in terms of temperature anomalies, reducing the magnitude of the features at shallower depths and increasing their magnitude at greater depths. The structural features in lower mantle tomographic models now in terms of temperature appear markedly similar to com-

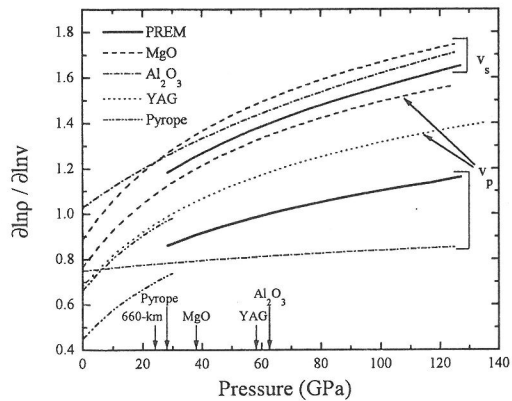


FIG. 11. Plot of  $(\partial \ln \rho / \partial \ln v)_T$  versus pressure at room temperature for four of the five minerals of this study. The YAG shear velocity values are off the scale (see Table 3) since  $v_s$  changes very little with pressure. The adiabatic PREM values at lower mantle pressures and temperatures (DZIEWONSKI and ANDERSON, 1981) are included in the figure for comparison. The highest pressure attained in each of the experiments for the four minerals are indicated on the pressure axis. The extrapolated values for three of the four minerals were obtained by assuming a linear velocity-volume relationship (see Table 1). The values for pyrope are shown only to 28 GPa since a change in compressional mechanism is observed here (see Fig. 8b).

Table 3. Values of the density dependence of  $(\partial \ln \rho / \partial \ln v)_T$  for five minerals.

	$(\partial \ln \rho / \partial \ln v_s)_T$	$(\partial \ln \rho / \partial \ln v_p)_T$
MgO	$0.85 + 3.7 \cdot \ln(\rho/\rho_0)$	$0.76 + 1.9 \cdot \ln(\rho/\rho_0)$
MgAl <sub>2</sub> O <sub>4</sub> *	$\approx \infty$	$0.97 + 11 \cdot \ln(\rho/\rho_0)$
Al <sub>2</sub> O <sub>3</sub>	$1.03 + 2.5 \cdot \ln(\rho/\rho_0)$	$0.75 + 0.39 \cdot \ln(\rho/\rho_0)$
Pyrope*	$0.67 + 2.7 \cdot \ln(\rho/\rho_0)$	$0.46 + 2.4 \cdot \ln(\rho/\rho_0)$
YAG	$3.3 + 5.5 \cdot \ln(\rho/\rho_0)$	$0.69 + 2.7 \cdot \ln(\rho/\rho_0)$

\*pyrope values to 28 GPa and MgAl<sub>2</sub>O<sub>4</sub> values to 11 GPa

puter simulations of plumes (YUEN *et al.*, 1993), which supports the hypothesis that  $(\partial \ln \rho / \partial \ln v)_P$  increases with depth.

The results obtained here are insufficient to determine the exact value of the thermal anomalies because the anelastic contribution to  $(\partial \ln \rho / \partial \ln v)_P$  is not known. There is evidence that the anelastic contribution may be as significant as the elastic (anharmonic) contribution, and thus will reduce the value of  $(\partial \ln \rho / \partial \ln v)_P$  (KARATO, 1993) and which, in turn, reduces the calculated thermal anomaly.

### CONCLUSIONS

Sound velocities of five minerals measured using the new sideband method have been presented and are shown to be in excellent agreement with the lower pressure results obtained by other methods. This means that the acoustic modes measured here yield spherically averaged information. We find that the velocity is linear with volume as long as no phase change or change in compressional mechanism occurs. However, this velocity-volume function varies from mineral to mineral and is smaller for minerals with significant alumina contents, particularly for the shear velocity. The linear velocity-volume relationship requires that  $(\partial \ln \rho / \partial \ln v)_T$  increase with pressure or decreasing volume. Since the intrinsic anharmonicity decreases with depth, the isobaric  $(\partial \ln \rho / \partial \ln v)$  must also increase with depth. This in turn increases the magnitude of the calculated thermal anomalies from the seismic tomographic velocity anomalies with depth.

*Acknowledgments*—Partial support for L. Zhang and H. R. Reichmann was provided by the Bundes Ministerium für Forschung und Technik (BMFT). A. Zerr assisted in the CO<sub>2</sub> laser heating of MgO and Al<sub>2</sub>O<sub>3</sub> samples. Critical comments by G. C. Serghiou, R. Boehler, A. M. Hofmeister, and O. L. Anderson improved the manuscript.

### REFERENCES

- ANDERSON O. L., ISAAK D. and ODA H. (1992) High-temperature elastic constant data on minerals relevant to geophysics. *Rev. Geophys.* **30**, 57–92.
- BIRCH F. (1978) Finite strain isotherm and velocities for single crystal and polycrystalline NaCl at high pressures and 300 K. *J. Geophys. Res.* **83**, 1257–1268.
- CAMPBELL A. J. and HEINZ D. L. (1992) A high-pressure test of Birch's law. *Science* **257**, 66–68.
- CHAI M., BROWN J. M. and SLUTSKY L. J. (1993) The elasticity of pyrope garnet to 22 GPa (abstract). *EOS, Trans. Am. Geophys. U.* **74**, 676.
- CHANG Z. P. and BARSCH G. R. (1973) Pressure dependence of single-crystal elastic constants and anharmonic properties of spinel. *J. Geophys. Res.* **78**, 2418–2433.
- CHOPELAS A. (1991) Evidence of a pressure-induced phase transition in tetragonal majorite: implications for the mantle (abstract). *EOS, Trans. Am. Geophys. U.* **72**, 478.
- CHOPELAS A. (1992) Sound velocities of MgO to very high compression. *Earth Planet. Sci. Lett.* **114**, 195–192.
- CHOPELAS A. (1996) The fluorescence sideband method for obtaining acoustic velocities at high compressions: Application to MgO and MgAl<sub>2</sub>O<sub>3</sub>. *Phys. Chem. Minerals*, **23**, 25–37.
- CHOPELAS A. and BOEHLER R. (1992) Thermal expansivity in the lower mantle. *Geophys. Res. Lett.* **19**, 1983–1986.
- CHOPELAS A. and HOFMEISTER A. M. (1991) Vibrational spectroscopy of aluminate spinels at 1 atm and of MgAl<sub>2</sub>O<sub>4</sub> to over 200 kbar. *Phys. Chem. Minerals* **18**, 279–293.
- CHOPELAS A. and NICOL M. F. (1982) Pressure dependence to 100 kbar of the phonons of MgO at 90 and 295 K. *J. Geophys. Res.* **87**, 8591–8597.
- DUFFY T. S. and AHRENS T. J. (1995) Compressional sound velocity, equation of state, and constitutive response of shock-compressed magnesium oxide. *J. Geophys. Res.* **100**, 529–542.
- DZIEWONSKI A. M. and ANDERSON D. L. (1981) Preliminary reference Earth model. *Phys. Earth Planet. Inter.* **25**, 297–356.
- GIESKE J. H. and BARSCH G. R. (1968) Pressure dependence of the elastic constants of single crystal aluminum oxide. *Phys. Stat. Solidi* **29**, 121–131.
- GLASS A. M. and SEARLE T. M. (1967) Reactions between vacancies and impurities in magnesium oxide. II. Mn<sup>4+</sup>-

- ion and OH<sup>-</sup>-ion impurities. *J. Chem. Phys.* **46**, 2092–2101.
- GOTO T., YAMAMOTO S., OHNO I. and ANDERSON O. L. (1989) Elastic constants of corundum up to 1825 K. *J. Geophys. Res.* **94**, 7588–7602.
- HARDY R. J. (1980) Temperature and pressure dependence of intrinsic anharmonic and quantum corrections to the equation of state. *J. Geophys. Res.* **85**, 7011–7015.
- HOFMEISTER A. M. and CAMPBELL K. R. (1992) Infrared spectroscopy of yttrium aluminum, yttrium gallium, and yttrium iron garnets. *J. Appl. Phys.* **72**, 638–646.
- HOFMEISTER A. M. and CHOPELAS A. (1991) Vibrational spectroscopy of end-member silicate garnets. *Phys. Chem. Minerals* **17**, 503–526.
- HURRELL J. P., PORTO S. P. S., CHANG I. F., MITRA S. S. and BAUMAN R. P. (1968) Optical phonons of yttrium aluminum garnet. *Phys. Rev.* **173**, 851–858.
- ISAAK D. G., ANDERSON O. L. and GOTO T. (1989) Measure elastic modulus of single-crystal MgO up to 1800 K. *Phys. Chem. Minerals* **16**, 703–714.
- JACKSON I. and NIESLER H. (1982) The elasticity of periclase to 3 GPa and some geophysical implications. *High Pressure Research in Geophysics*. (ed. S. AKIMOTO and M. H. MANGHNANI) Tokyo. pp. 98–113. Center of Academic Publications of Japan.
- KAPPUS W. (1975) Lattice dynamics of sapphire (corundum), part II: calculation of the phonon dispersion. *Z. Physik* **B21**, 325–331.
- KARATO S. I. (1993) Importance of anelasticity in the interpretation of seismic tomography. *Geophys. Res. Lett.* **20**, 1623–1626.
- KITTEL C. (1976) *Introduction to Solid State Physics*. John Wiley & Sons, Inc.
- O'NEILL B., BASS J. D., ROSSMAN G. R., GEIGER C. A. and LANGER K. (1991) Elastic Properties of Pyrope. *Phys. Chem. Minerals* **17**, 617–621.
- SANGSTER M. J. L., PECKHAM G. and SAUNDERSON D. H. (1970) Lattice dynamics of magnesium oxide. *J. Phys. C* **3**, 1026–1036.
- SPEZTLER H., SAMMIS C. G. and O'CONNELL R. J. (1972) Equation of state of NaCl: Ultrasonic measurements to 8 kbar and 800°C and static lattice theory. *J. Phys. Chem. Solids* **33**, 1727–1750.
- THOMPSON P. and GRIMES N. W. (1978) Observation of low energy phonons in spinel. *Solid St. Comm.* **25**, 609–611.
- WEBB S. L. (1989) The elasticity of the upper mantle orthosilicates olivine and garnet to 3 GPa. *Phys. Chem. Minerals* **16**, 684–692.
- WEIDNER D. J., WANG Y. and YEGANEH-HAERI A. (1993) Equation of state properties of mantle perovskite (abstract). *EOS, Trans. Am. Geophys. U.* **74**, 571.
- YAMAMOTO S. and ANDERSON O. L. (1987) Elasticity and anharmonicity of potassium chloride at high temperature. *Phys. Chem. Minerals* **14**, 332–340.
- YAMAMOTO S., OHNO I. and ANDERSON O. L. (1987) High temperature elasticity of sodium chloride. *J. Phys. Chem. Solids* **48**, 143–151.
- YOGURTCU Y. K., MILLER A. J. and SAUNDERS G. A. (1980) Elastic behavior of YAG under pressure. *J. Phys. C: Sol. St. Phys.* **13**, 6585–6597.
- YONEDA A. (1990) Pressure derivatives of elastic constants of single crystal MgO and MgAl<sub>2</sub>O<sub>4</sub>. *J. Phys. Earth* **38**, 19–55.
- YUEN D. A., CADEK O., CHOPELAS A. and MATYSKA C. (1993) Geophysical evidences for thermal chemical plumes in the lower mantle. *Geophys. Res. Lett.* **20**, 899–903.
- ZHANG L. and CHOPELAS A. (1994) Sound velocity of Al<sub>2</sub>O<sub>3</sub> to 616 kbar. *Phys. Earth Planet. Inter.* **98**, 77–83.